In situ fate of Chikungunya virus replication organelles

Justine Girard, Olivier Le Bihan, Joséphine Lai-Kee-Him, Maria Girleanu, Eric Bernard, Cedric Castellarin, Matthew Chee, Aymeric Neyret, Danièle Spehner, Xavier Holy, et al.

In situ fate of Chikungunya virus replication organelles

Justine Girard[1,2], Olivier Le Bihan[3], Joséphine Lai-Kee-Him[1], Maria Girleanu[3], Eric Bernard[2], Cedric Castellarin[3], Matthew Chee[1], Aymeric Neyret[2], Danièle Spehner[3], Xavier Holy[3], Anne-Laure Favier[3], Laurence Briant[2*] and Patrick Bron[1*]

[1] CBS (Centre de Biologie Structurale), Université de Montpellier, CNRS, INSERM, Montpellier, France.

[2] IRIM (Institut de Recherche en Infectiologie de Montpellier), Université de Montpellier, CNRS, Montpellier, France.

[3] IRBA (Institut de Recherche Biomédicale des Armées), Ministère des armées, Brétigny-sur-Orge, France.

* For correspondence: Laurence Briant (laurence.briant@irim.cnrs.fr), Patrick Bron (patrick.bron@cbs.cnrs.fr)

Disclosure Statement

The authors declare they have no competing interests or disclosures.

Keywords: Alphavirus, Chikungunya, Replication organelles, nsP1, cryogenic-electron microscopy, sub-tomogram averaging, electron tomography, CEMOVIS.

Abstract

Chikungunya virus (CHIKV) is a mosquito-borne pathogen responsible for an acute musculoskeletal disease in humans. Replication of the viral RNA genome occurs in specialized membranous replication organelles (RO) or spherules, containing the viral replication complex. Initially generated by RNA synthesis-associated plasma membrane deformation, alphavirus ROs are generally rapidly endocytosed to produce type I cytopathic vacuoles (CPV-I) from where nascent RNAs are extruded for cytoplasmic translation. By contrast, CHIKV ROs are poorly internalized, raising the question of their fate and functionality at late stage of infection. Here, using *in situ* cryogenic-electron microscopy approaches, we investigate the outcome of CHIKV ROs and associated replication machinery in infected human cells. We evidence the late persistence of CHIKV ROs at the plasma membrane with a crowned protein complex at the spherule neck similar to the recently resolved replication complex. The unexpectedly heterogeneous and large diameter of these compartments suggests a continuous dynamic growth of these organelles beyond the replication of a single RNA genome. Ultrastructural analysis of surrounding cytoplasmic regions supports that outgrown CHIKV ROs remain dynamically active in viral RNA synthesis, and export to the cell cytosol for protein translation. Interestingly, rare ROs with a homogeneous diameter are also marginally internalized in CPV-I near honeycomb-like arrangements of unknown function, which are absent in uninfected controls, thereby suggesting a temporal regulation of this internalization. Altogether, this study sheds new light on the dynamic pattern of CHIKV ROs and associated viral replication at the interface with cell membranes in infected cells.

Importance

The Chikungunya virus (CHIKV) is a positive-stranded RNA virus requiring specialized membranous replication organelles (ROs) for its genome replication. Our knowledge of this viral cycle stage is still incomplete, notably regarding the fate and functional dynamics of CHIKV ROs in infected cells. Here, we show that CHIKV ROs are maintained at the plasma membrane beyond the first viral cycle, continuing to grow and to be dynamically active both in viral RNA replication and in its export to the cell cytosol where translation occurs in proximity to ROs. This contrasts with the homogeneous diameter of ROs during internalization in cytoplasmic vacuoles, which are often associated with honeycomb-like arrangements of unknown function, suggesting a regulated mechanism. This study sheds new light on the dynamics and fate of CHIKV ROs in human cells and, consequently, on our understanding of the Chikungunya viral cycle.

Introduction

Positive-strand RNA viruses replicating in the host cytoplasm dramatically remodel intracellular membranes into specialized vesicular structures supporting viral RNA genome replication and transcription (1–3). Generally separated from the cytoplasm by a proteinaceous pore, these viral replication organelles (RO) provide an optimal microenvironment that concentrates metabolites and viral and host components required for genome replication. They are also supposed to shield double-stranded RNA (dsRNA) replication intermediates from innate immune sensors and antiviral effectors and may additionally coordinate genome replication, viral translation, and new particle assembly (4, 5). Deciphering the organization, biogenesis, and mechanisms of maintenance of ROs at the molecular level, therefore represents an area of intense interest with potential consequences for therapeutic intervention. Recent advances in cryogenic-electron microscopy (cryo-EM) and cryogenic-electron tomography (cryo-ET), sub-tomogram averaging and 3D reconstruction techniques have been instrumental in elucidating the 3D volume architecture of ROs assembled by a variety of pathogenic RNA viruses (e.g. nodaviruses, flaviviruses, bromoviruses, tombusviruses, coronaviruses) (6–13). Contrasting with this significant breakthrough, our knowledge of alphavirus ROs has long lagged behind that of other positive-stranded RNA viruses.

Alphaviruses (*Togaviridae* family) are mosquito-borne viruses that can cause severe human illnesses including persistent arthritis and fatal encephalitis. Among these, the Chikungunya virus (CHIKV), responsible for severely debilitating and often chronic rheumatic disease, has become a major public health issue, notably due to the rapid spreading of its mosquito vectors *Aedes aegypti* and *Aedes albopictus* (14–17). CHIKV is an enveloped virus of about 50-60 nm in diameter (18). Since it re-emerged at the beginning of the 2000s, its multiplication cycle has been the focus of intense attention, resulting in the following picture (19, 20). The

CHIKV particle is internalized in endosomes where the fusion of viral and cell membranes occurs to release the nucleocapsid in the cytoplasm (21). After uncoating, the replication is initiated when the viral genome, a positive-sense single-stranded RNA molecule of 11.8kb containing a 5'-cap and a 3' polyadenylated tail is loaded by the host translation machinery. The 5'-proximal two-thirds of the viral genome corresponding to the first open reading frame (ORF) is translated into a non-structural polyprotein precursor (P1234) which associates with an RNA genome and is trafficked to the plasma membrane (22). P1234 sequential proteolytic processing results in the release of the four non-structural proteins, which assemble to form the viral replicase: nsP1, the methyl- and guanylyltransferase which ensures the viral RNA 5′ cap synthesis and plasma membrane (PM) anchoring of the replication complex (2, 23); nsP2, the RNA helicase and cysteine protease responsible for polyprotein autoprocessing which also displays 5'-RNA triphophatase activity (24, 25); nsP3, which contains an ADP-ribosyl binding and hydrolase activity (26) and associates with essential proviral cell factors (27); nsP4, the RNA-dependent RNA polymerase (RdRp) (28). This complex replicates the RNA genome (gRNA) through the synthesis of a negative-strand RNA template ((-)RNA), resulting in the accumulation of double-stranded RNA (dsRNA) replication intermediate species (29, 30). Starting from the (-)RNA, CHIKV replicase also controls the transcription of a 26S subgenomic RNA (sgRNA) corresponding to the 3' ORF, translated into five structural proteins: capsid (C), envelope and surface glycoproteins (E1, E2, E3), and 6K/TF required to form the nascent viral particle.

Alphavirus genome replication and transcription take place in bulb-shaped ROs in which the replication complex (RC) is anchored to the lipid bilayer by a dodecameric ring of nsP1 (31, 32). The proteinaceous pore, 14 nm in diameter with a central pore of 7.5 nm, formed by this monotopic protein with affinity for anionic lipids and cholesterol-rich microdomains (33–36) could contribute to the structural maintenance of replication compartments while ensuring the

simultaneous capping of the multiple newly synthesized RNA molecules trafficked through this pore to the cytosol for translation or transport to assembly sites.

The biogenesis and activity of alphavirus ROs are temporally regulated processes. Noninfectious trans-replication systems revealed that ROs primarily emerge from the plasma membrane of the infected cell when the fully active RdRp nsP4 is released from the P1234 polyprotein, thereby activating the synthesis of the (-)RNA strand (1, 2, 7, 37–39). Further cleavage of the early replicase into a short-lived nsP1+P23+nsP3 complex converts replicase activity and promotes the synthesis of positive gRNA inside ROs. The final processing of P23 results in a fully mature replicase mainly transcribing sgRNA. At this stage, RO size strictly depends on the size and amount of RNA in these compartments. For some alphaviruses (e.g. Semliki Forest virus and Sindbis virus) these compartments are endocytosed and fused with endosomes (2, 38, 39). The resulting cytosolic vacuolar structures, referred to as type I cytopathic vacuoles (CPV-I) support nascent RNA export for cytoplasmic translation. Contrasting with this picture, CHIKV ROs persist at the plasma membrane, therefore prompting us to question the dynamics of associated viral replication events (40).

In the present work, we have investigated CHIKV spherules structural organization in their cellular context using *in situ* cryogenic-electron microscopy (cryo-EM), combined with a sub-tomogram averaging approach. To access a dynamic view of the CHIKV replication cycle, the infected cells from fully replicative infectious CHIKVs were imaged at 17h post-infection (hpi), a late time point encompassing a second and possibly a third CHIKV replication cycle that is 6-8h long. We observed CHIKV ROs as single membrane vesicles in continuity with the plasma membrane, present both on the cell body and filopodia-like extensions. Contrasting with previous electron microscopy observations performed after one viral cycle (6-8h of infection), ROs exhibited a wide range of diameters. In addition, we also observed that a portion of ROs, with a smaller and more homogeneous diameter, were internalized into

cytosolic vacuoles. A detailed examination of ROs revealed the presence of a thicker density at the spherule neck and additional densities extending into the cytoplasm. Associated with some structures, we visualized the presence of extruding filaments, sometimes covered with small globular densities resembling viral RNA tightly associated with ribosomes evoking a possible CHIKV translating activity at the plasma membrane. The sub-tomographic averaging of ROs at the PM provides evidence for a proteinaceous complex at the neck strongly interacting with the PM lipid bilayer, compatible with nsP1 dodecameric ring assembled *in vitro* (31, 32, 41) and provides additional details for the organization of CHIKV ROs in human cells.

Materials and Methods

Cell culture

Human Embryonic kidney (HEK293T, ATCC #ACS-4500) and BHK-21 cells (ATCC #CCL-10) were used for viral propagation. African green monkey (Vero ATCC #CCL-81) cells were used for viral titration. All cells were cultured in Dulbecco modified Eagle medium (DMEM, Thermo Fisher Scientific) supplemented with Penicillin-Streptomycin 1%, fetal calf serum 10% (FCS, Sigma-Aldrich) and grown at 37°C, in a 5% CO_2 atmosphere.

Virus stock production

The pCHIKV-LR-3'GFP (LR-OPY1 isolate) and the CHIKV-377-mCherry (BNI-CHIKV_899 isolate) full-length molecular clones containing GFP and m-cherry reporters respectively (34, 42, 43) were transcribed *in vitro* using the mMESSAGE mMACHINE SP6 kit (Invitrogen, AM1340) and the mMESSAGE mMACHINE T7 kit (Invitrogen, AM1344) respectively, following manufacturer's instructions. RNA (1µg) was then transfected with Lipofectamine 2000 (Thermo Fisher Scientific) into 10^5 HEK293T cells and incubated at 37°C 5% CO_2 for 24h. The supernatant was harvested, and the virus stock was amplified using BHK-21 cells. After 48h culture, the supernatant was collected, filtered through 0.45µm, aliquoted and stored at -80°C. Viral stocks were titrated using Vero cell plaque assays as previously described (44). The virus assays were performed under BSL-3 safety conditions.

Immunofluorescence assay

HEK293T cells grown on a glass coverslip and CHIKV-challenged for 17h at MOI of 50 were fixed with 4% formaldehyde/PBS (Sigma-Aldrich) for 30 min, then washed with PBS 1X, permeabilized with 0.1% Triton X-100 and blocked in PBS–2% fetal calf serum (FCS) for 45 min. Incubation with primary antibodies (nsP1 and dsRNA) was performed for 2h at room

temperature (RT), followed by incubation of Alexa-488 / -647 secondary antibodies also for 2h at RT. nsP3 is detected through the fluorescence of the fused *mCherry* protein. Nuclei were stained with DAPI (4′,6′-diamidino-2-phenylindole; Sigma-Aldrich). After the final washes, coverslips were mounted with ProLong Gold antifade reagent (Invitrogen). Images were acquired using an Ayriscan super-resolution microscope (Confocal Zeiss LSM880 Airyscan) at the Montpellier Resources Imaging (MRI) platform. Image processing and colocalization analysis were performed using ImageJ software (45).

EM thin sections

HEK293T cells were infected with CHIKV for 17h at a MOI of 50 and then pelleted and fixed in 2.5% glutaraldehyde sodium cacodylate buffer for 1h. After a brief wash, cell pellets were post-fixed into 1% osmium solution for 1h and processed for successive dehydration steps in several ethanol baths. Blocks of polymerized resin were cut into thin slices of 80 nm with an ultramicrotome. Thin slices were placed on EM copper grids, stained with 2% Uranyl Acetate and imaged using a 120kV JEM-400 Flash electron microscope (JEOL).

Sample preparation – cryo-EM

Cells were cultured directly on gold grids (R2/1, carbon film, Quantifoil) after being glow-discharged using a Pelco GD system. HEK293T cells were infected at the MOI of 50 for 17h in the growing medium and then fixed with 4% paraformaldehyde (PFA). After a brief wash with PBS, grids were loaded on the Mark IV Vitrobot system tweezers (FEI). 3 µL of 10 nm BSA-treated fiducial gold particles (BBI solutions) were added on both sides of the grid before blotting for 22 seconds with Whatman paper at a -5 force offset. The chamber was kept at 100% humidity and room temperature. Grids were then rapidly plunge-frozen in nitrogen-cooled liquid ethane and stored in liquid nitrogen until imaged.

Electron microscope setup – tilt series acquisition

For cryo-data acquisition, we used a Titan Krios cryo-TEM equipped with a field emission gun, operating at 300 kV (IRBA, Institut de Recherche Biomédicale des Armées, Brétigny-sur-Orge, France). Images were recorded on a Falcon III direct electron detector (Thermo Fisher Scientific). Regions of interest were recorded using MAPS software (Thermo Fisher Scientific). Tomographic tilt series were acquired with Tomo4 (Thermo Fisher Scientific) at a magnification of 29,000 × and exposed for 1.3-1.55 seconds, with a pixel size of 2.931 Å using continuous focusing and tracking controls. Tomograms were collected with a 2° tilt increment for a range spanning from −60° to +60° according to a dose symmetric acquisition tilt scheme (46), using defocus values ranging from -3 to -12 µm. The total electron dose per tomogram was between 65 and 75 electrons/Å^2.

Tomographic reconstruction

In general, tomograms were reconstructed similarly as described elsewhere (47). Movies were firstly motion-corrected and averaged using the *MotionCorr* software (48). Tomogram reconstruction was then performed with Etomo from IMOD (49). The tilt series were coarsely aligned using cross-correlation. CTF curves were estimated with *CtfPlotter* implemented in IMOD (50, 51). To remove the contribution of high-frequency information loss due to cumulative beam damage at high tilt angle, dose weighing was performed (52) using the *MtfFilter* function of IMOD. The tomograms were reconstructed alternatively by weighted back-projection (WBP) and by SIRT (simultaneous iterations reconstruction technique) using 8 iterations and were subsequently binned by 2, resulting in pixel sizes of 5.862 Å. To further facilitate visualization, a non-linear anisotropic diffusion (NAD) filter provided by IMOD is applied to the 2 times binned tomograms. Segmentation and animation were done using Amira software (Thermo Fisher Scientific).

Sub-Tomogram averaging

All sub-tomogram averaging (STA) steps were performed using the EMAN2 package (53, 54) in version 2.9.9 unless stated otherwise. Masks were created with the EMAN2 e2filtertool.py and e2proc3d.py programs.

Pre-processing. Movie fractions were motion-corrected using MotionCor2 (48) to compensate for beam-induced sample motion. A custom Python script was used to automate that process and build a motion-corrected tilt-series stack, relying on the newstack and clip programs from the IMOD package (49).

Tilt-series alignment. A total of 38 tilt-series were aligned using the EMAN2 landmark-based iterative approach and CTF estimation was performed. Low-pass filtered, binned by 4 tomograms were reconstructed for visualization and particle picking only.

Particle picking and extraction. We repurposed the e2tomo_drawcurve.py boxer program, originally designed to pick particles along filaments to pick orientation-aware spherule particles on bin 4 tomograms. Two points (3D coordinates) were assigned to each particle deemed suitable for analysis. One point was placed at the estimated center of the spherule neck and designated the center of the particle to be extracted. A second point was set inside the spherule compartment, towards its main axis as a way to manually assign an approximate orientation to the particle. Those coordinates were stored in .json files. Stacks of per-particle CTF corrected 2D sub-tilt-series were extracted and corresponding 3D sub-tomograms reconstructed at binning 4 using e2spt_extract.py. The --curves option was set to read the particle orientation metadata and encode it in the extracted particle stacks header. The e2spt_extract.py script was modified so that it accepts particles with only 2 points defined and avoids doing any coordinates interpolation. A total of 463 binning 4 particles, 384 unbinned pixels in size were extracted from 38 tilt-series.

Initial model generation. A low-resolution initial model was generated at binning 8 using the iterative stochastic gradient descent (SGD) approach implemented in e2spt_sgd.py. Initial

particle orientations read from their header were used as a seed for refinement. C57 symmetry was imposed during alignments as a way to improve the signal-to-noise ratio and force any rotational symmetry around the spherule main axis without applying any specific symmetry order. C1 refinements did not reveal obvious natural symmetry in the data, therefore we carried on using C57 symmetry for the downstream processing steps.

Model refinement and classification. Gold-standard single model refinements were done using the e2spt_refine_new.py program while multi-reference refinements employed e2spt_refinemulti_new.py. A first refined model was generated at binning 4 taking the initial model as a reference and using a large soft spherical mask, 192 unbinned pixels in diameter, for alignment. Particle orientations were refined within a search range of 16 degrees around their initial orientations determined at picking time. A first round of classification by iterative multi-reference refinement was performed using the same mask. Three references were initialized by randomly splitting particles into three sub-sets and averaging them. One class containing 166 particles was selected for further refinement. Particles belonging to that class were re-extracted at binning 2, with a size of 256 unbinned pixels, and a new model was refined from them. To tackle the remaining heterogeneity in the data, a second round of classification without alignment was performed inside a tighter soft threshold-based mask. Out of the four classes, the major class containing 98 particles was further refined inside a similar tight mask using both traditional iterations of 3D particle alignment refinement and 2D sub-tilt refinement with C57 symmetry applied. A last alignment round was performed with no symmetry applied and a pseudo-randomization of rotations around the axis of symmetry (azymuth) in order to mitigate the effects of the missing wedge. The visualization of 3D reconstruction was performed using UCSF Chimera (developed by the Resource for Biocomputing, Visualization, and Informatics at the University of California, San Francisco, with support from NIH P41-GM103311) (55).

Validation and post-processing. The gold-standard Fourier shell correlation (FSC) curve calculated from two independently refined half-maps using the same mask as the one used for refinement indicates an estimated resolution of the un-symmetrized map of 31 Å at FSC=0.143. The final map was Wiener filtered by the masked FSC.

High-pressure freezing and vitreous sectioning

CHIKV-infected HEK293T cells were inactivated in 2.5% glutaraldehyde and 20% dextran-sodium cacodylate 0.1M (Delta Microscopies). Pellets were frozen on copper tube carriers using the EM ICE high-pressure freezer (HPF, Leica). After HPF, the sample was processed by CEMOVIS (Cryo-Electron Microscopy of Vitreous Sections). Vitreous sectioning was performed on infected cell tubes containing the vitrified sample pre-cooled at -140°C on an EM UC6/ FC7 cryo-ultramicrotome (Leica Microsystems). The sample was trimmed to a pyramidal-shaped block of 140 µm base and approximately 50 µm height using a 45° cryo-trimming diamond knife (CT441; Diatome). A cryo immuno diamond knife (MT15692; Diatome) with a clearance angle of 6° was used to get ribbons of cryo-sections at a nominal cutting feed of 50 nm and cutting speeds of 40 mm/s. Ribbons of cryo-sections were attached to a pre-cooled copper grid (hexagonal, 100 mesh with carbon and formvar). All samples were analyzed on the IRBA Titan Krios microscope operated at 300 kV using a Falcon III detector in linear mode. The microscope was set to nanoprobe mode with 50 µm C2 aperture at 47,000X magnification corresponding to 1.81 Å/pixel. TIA ® was used to acquire images using defocus values ranging from -3 µm to -5 µm with an average cumulative dose of 17.7 e^- /$Å^2$.

Data availability

The 3D reconstruction of the CHIKV complex at the base of replication organelles was deposited in the Electron Microscopy Data Bank (EMDB) with the accession number EMD-50321.

Results

CHIKV replication sites preferentially localize at the plasma membrane of human epithelial cells

Alphavirus ROs, which concentrate the four virus-encoded nsPs and viral double-stranded RNA (dsRNA) are first assembled at the plasma membrane (PM) of the infected host cell, and later internalized and fused with endosomal compartments to produce type-1 cytopathic vacuoles (56). We first questioned the localization of CHIKV replication sites in the virus-permissive HEK293T epithelial cell line infected with a reporter virus (BNI-CHIKV_899 strain) containing a mCherry coding sequence in nsP3 hypervariable domain (42). To increase the probability of detecting replication events, we used an MOI of 50, and to access the different replication steps the cells were infected for 17h, a duration that allows several replication cycles (estimated for alphavirus around 6-8h) to occur (Fig. S1) (16, 57). At this time point, around 40% of the cells showed no sign of death (not shown). Focusing on cells with an unaltered morphology, replication sites were identified by immunostaining of nsP1 and 3 together with dsRNA, which represents a good RO marker (39, 57, 58), and by confocal microscopy. Colocalized nsPs and dsRNA fluorescence signal is mainly detected at the plasma membrane (PM) (Fig. 1A; white arrows). Interestingly this signal is also observed in cellular extensions (Fig. 1A, yellow arrows), suggesting that replication compartments exist both on the cell body and at the PM delimiting virus-induced filopodia-like extensions, as previously reported in alphavirus-infected vertebrate cells (59). Finally, a minor fraction of dsRNA colocalizes with both nsP1 and nsP3 in cytosolic aggregates, supporting the claim that CHIKV replication complexes undergo some marginal endocytosis events as suggested (40). Electron microscopy of thin sections of CHIKV-infected HEK293T cells confirms the presence of CHIKV ROs at the plasma membrane as spherules with condensed genetic material (Fig. 1B, black arrows). Rare cytopathic vacuoles can be observed (Fig. 1D and E)

often associated with a regular honeycomb-like network of densities containing globular and tubular densities (Fig. 1 E, F, red and blue arrows). According to these characteristics, CHIKV replication sites detected at the plasma membrane are suitable for cryo-EM investigation.

Cryo-electron tomography of CHIKV ROs located on the cell body and filopodia-like extensions of infected cells

HEK293T cells were directly grown onto gold EM grids, infected with CHIKV, subsequently inactivated with 4% PFA fixation and embedded in vitreous ice. Compared to confocal experiments, we increased cell density to maintain sufficient cells onto grids after their freezing, still keeping a high multiplicity of infection (MOI 50) and 17h of CHIKV infection. Inspection of EM grids readily reveals the presence of well-preserved frozen-hydrated infected cells at this infection time, as evidenced by the continuous delineation of their plasma membrane (Fig 2A). We collected more than 300 cryo-tomographic tilt series of the infected cell peripheries that were processed in Etomo (49) and segmented using Amira software (Thermo Fisher Scientific) (Fig. 2). These tomograms of CHIKV-infected cells are in agreement with confocal observations, revealing the presence of CHIKV ROs both on HEK293T cell bodies and on their numerous filopodia-like extensions (Fig 2A, C and E). ROs appear as clusters of round vesicles of variable diameter covering the PM (Fig 2, orange arrows). They are delimited by a lipid bilayer connected to the PM through a narrow neck (Fig. 2, white arrows). Analysis of the spherules' contents shows that all compartments imaged contain a compactly coiled filamentous density corresponding to dsRNA packed inside (Fig 2E, F, light blue arrows) as previously observed for nodavirus ROs (7). No additional inner density is observed, indicating the absence of an internal coat contributing to membrane curvature. Contrasting with this appearance, CHIKV virions are observed as spherical particles of about 50-60 nm in diameter, highly electron-dense, and covered by

protruding densities (Fig. 2C, E, red arrows). In the present study, most CHIKV replication spherules are located at the PM delimiting the cell body of infected cells (Fig. 2A) whereas filopodia-like extensions exhibited some ROs colocalized with most CHIKV budding particles (Fig. 2C and E).

The computed 3D reconstructions granted us access to cellular structural details of ROs' local cellular environment, notably revealing the presence of cytoskeleton filaments (Fig. 2, purple arrows) or cell host factors (Fig 2, green arrows). When both ice thickness and defocus values used during the tilt series acquisitions are low, the level of detail observed in images can be high. Thus, it is possible to discriminate the double-layer organization of the plasma membrane or observe the repetitive nature of actin filaments present in filopodia-like extensions (Fig. 2C, brown arrows and inset), some good indicators of the dataset's intrinsic resolution. It is worth noting that CHIKV infection induces local cellular rearrangement. While filopodia normally appear as cellular extensions containing a continuous bundle of parallel actin filaments in close contact with the PM, actin filaments in CHIKV-induced filopodia-like extensions bearing ROs and/or CHIKV viral particles are separated from the PM by a space where cellular components like ribosomes accumulate (Fig. 2C versus SFig. 1). This phase separation suggests a cellular activity that certainly relies on the CHIKV viral cycle, possibly associated with the production and assembly of viral particles. Indeed, as illustrated in Fig. 2E, filopodia-like extensions also display CHIKV budding sites near ROs, often associated with a thickening of the PM (Fig. 2E, dark blue arrows), a characteristic recently correlated to the insertion of immature envelope spikes in the lipid bilayer (60). Furthermore, ROs from the aforementioned region bear some extra densities protruding out of their membrane (Fig. 2E, yellow arrows). Considering their proximity to budding sites, these densities likely correspond to CHIKV envelope glycoproteins. This unexpected feature agrees

with recent immuno-labeling experiments of CHIKV-infected cells with anti-E2 antibodies reported by Jin et al. (61), revealing some signals at the surface of ROs.

CHIKV ROs display variable size distribution

Alphavirus ROs have been initially reported to display a standard diameter of around 50 nm (1, 62). As mentioned above, CHIKV replication compartments detected in our experiments primarily appeared unexpectedly heterogeneous in size (Fig. 2A), an observation also validated by CHIKV-infected cells plastic sections (Fig. 1B and C). To provide objective validation for this observation, we measured the diameter of over 3000 ROs from cryo-tomograms. As ROs can be elongated perpendicularly to the PM, we considered the maximal diameter of ROs parallel to the PM (inset Fig. 3A). In this context, we determined the diameters of 2,083 and 950 ROs from PM of cell bodies and filopodia-like extensions respectively and plotted them as a histogram representation (Fig. 3). RO diameters display a Gaussian distribution ranging from 40 to 140 nm with a mean of 84.2 nm and 90 nm for ROs located at the PM of cell bodies and filopodia-like extensions respectively (Fig. 3A). Thus, we only observed a slight shift of the mean diameter between ROs localized on the PM of cell bodies and filopodia. It is worth noting that we never observed ROs with a diameter smaller than 40 nm. Moreover, the biggest ROs, having a diameter superior to 120 nm, are only found on the cell bodies. While these observations support that ROs assembled at the PM of cell bodies can be slightly bigger than those detected on filopodia, this feature is not entirely clear, especially due to the overall unexpected size variability of ROs observed in our experiments.

In a closer analysis of our data, considering the whole RO population, we discerned several RO diameter maxima of 55, 64, 74.5, 84, 91, 100, 122, and 139 nm (Fig. 3B), visually presenting a similar RNA compaction state inside spherules. It is worth noting that some very recent cryo-EM studies reported ROs with diameters of about 50 to 70 nm formed 6-8h after CHIKV infection (41, 63), a time point at which CHIKV's first replication cycle is considered

to be complete, resulting in the presence of mature ROs containing fully-processed nsPs and dsRNA replication intermediates, actively transcribing gRNA and sgRNA then exported for encapsidation and translation respectively. Previous molecular studies established that the volume of ROs and consequently their diameter tightly correlates with RNA genome length and indirectly with the size and amount of neosynthesized genetic material contained in these compartments (7, 38). Taking into account this information and the late time point considered in this study (17 hpi), we propose that ROs having a diameter superior to 80 nm may correspond to ROs in which viral RNA species continue accumulating. Therefore, the idea of a finite final size of ROs needs to be reconsidered according to the post-infection time.

CHIKV internalization in cytopathic vacuoles is regulated

Our confocal microscopy and electron microscopy analyses revealed that after a prolonged CHIKV infection, most ROs remain at the PM. To confirm this peculiarity and investigate the presence and structural organization of ROs internalized in CPVs, CHIKV-infected cells were processed according to the cryo-EM method of vitreous sectioning (CEMOVIS) (64). CPVs were rarely detected in vitreous sections, and usually in the vicinity of mitochondria (Fig. 4). They appear as vacuolar structures ranging from 200 to 500 nm in size, delineated by a lipid bilayer and housing spherules. From a morphological point of view, these organelles are similar to ROs located at the PM with a lipid membrane delimiting an internal area full of ball-of-yarn-like densities and connected to the CPV membrane envelope via a neck. No obvious additional density could be observed in the cytoplasm beneath these spherules. Although we did not observe it in our vitreous sections, CPVs are often associated with honeycomb arrangements never reported so far (Fig. 1D, E) (57). Contrasting with previous observations on related alphaviruses (1, 3, 57) showing spherules lining the CPVs, CHIKV spherules were found mostly disorganized in CPVs, a behavior confirmed by conventional electron microscopy of plastic sections (Fig. 1D, E). Interestingly, within CPVs, ROs display

418 a rather homogeneous diameter of about 50.6 nm ± 6 nm (Fig. 4), a rather surprising
419 observation when considering the heterogeneous size of those located at the PM. Considering
420 that large ROs at the PM may result from accumulated RNA at a late stage of infection, the
421 unexpected homogeneity in size and small diameter of ROs in CPVs argue for a temporally
422 regulated internalization mechanism susceptible to occur at a defined step of the CHIKV
423 replication cycle.

424 **Late CHIKV ROs exhibit heterogeneous patterns**

425 Considering the above-discussed RO size heterogeneity, the functionality of compartments
426 with an unexpected diameter poses an interesting question. In this context, we performed a
427 thorough inspection of our cryo-tomograms intending to report all different types of
428 molecular patterns of ROs, taking into account the size of these organelles and the presence or
429 absence of densities inside and immediately below spherules. In Fig. 5, we display different
430 sections of ROs and their corresponding segmentations according to their diameter, which
431 ranges from 50 to more than 120 nm. This exploration reveals that whatever the size of ROs,
432 the lumen of spherules is full of ball-of-yarn-like densities, with a state of compaction that
433 seems similar, suggesting a high RNA replication activity inside these compartments. It is
434 worth noting that all ROs display a density at the base of spherules, which gives the
435 impression that the PM is continuous with spherules sticking to it. Exploration of cytoplasmic
436 areas immediately beneath ROs revealed diverse patterns, varying from the absence of clear
437 associated densities below spherules (Fig. 5A; thumbnails 1 to 5) to the presence of compact
438 or filamentous densities extruding from ROs (Fig. 5B; thumbnails 6 to 12). These elongated
439 densities displaying various lengths ranging from 10 nm (Fig. 5, thumbnail 6) to more than
440 100 nm (Fig. 5, thumbnail 8-10, 12) are noticeable just beneath spherules, appearing like
441 extrusions from the replication compartment. Some of these filamentous objects are covered
442 by small globular densities, forming a sort of string of pearls (Thumbnail 8) reminiscent of

RNA covered with translating ribosomes as observed by colleagues (65), therefore suggesting a local translating activity. It is important to note that these long-exported viral RNA molecules were only observed for ROs larger than 90 nm in diameter. Moreover, when detected, only a single filament was observed beneath the spherule. Now, considering the base of the spherules, two elongated, short and parallel densities protruding in the cytoplasm, perpendicular to the PM plane and located on both sides of the neck can be observed under some spherules as in thumbnails 6 to 9 (in dark blue in segmentations). Finally, additional isolated globular densities are detected in cytoplasmic portions near the spherule, possibly attesting to the presence of viral proteins and/or cell host factors either translated in the vicinity of spherules or recruited to replication sites. Interestingly, no clear correlation could be made between these various intracytoplasmic features and RO size. Collectively, these different patterns of ROs deviating from the canonical 50-70 nm size range, strongly imply that beyond the expected completion of a single viral cycle, CHIKV ROs persist at the PM as enlarged spherules. This suggests ongoing and possibly continuous viral RNA synthesis in these compartments. Cytoplasmic regions beneath the spherules exhibit signs of RNA export and associated translation activities.

The CHIK ROs display a crown-like structural organization of the spherule neck

ROs assembled by (+)RNA viruses are thought to be connected to the cytoplasm by a pore complex localized at the spherule neck, allowing the import of metabolites and cell factors, and facilitating the export of newly synthesized viral RNA to the cytoplasm for translation and packaging (66). Some recent single particle analysis cryo-EM studies revealed that recombinant alphavirus nsP1 assembles into a dodecamer while in-situ cryo-ET on infected cells resolved similar structures and support the assembly of a connecting pore separating the inner part of the spherule from the cytoplasm (31, 32, 41, 63). We investigated the possibility

of transposing this model to our infected cultures at late replication stages. As mentioned above, we noticed the presence of a strong density at the base of each spherule neck, sometimes suggesting that the PM of the infected cell is continuous and that ROs are just sitting on top of it. To decipher the molecular organization of the connecting region, we developed a sub-tomogram averaging (STA) approach focused on the neck of ROs. The STA workflow is described in detail in Fig. S2. Briefly, a total of 463 sub-volumes were extracted and subjected to iterative alignment, averaging, and classification steps, applying full rotational symmetry as a way to help alignment of particles symmetry axis. Finally, symmetry was relaxed to produce an un-symmetrized map with an estimated resolution of 31 Å (gold standard FSC, FSC=0.143 threshold) from a final subset of 98 spherules. The dedicated use of masking and classification was instrumental in sorting out spherule neck morphological heterogeneity, such as variations in spherule diameter, neck length, curvature of the membrane at the base of the neck, as well as perpendicularity of spherule main axis to the PM plane. The bilayer organization of the membrane is distinctly evident in a central slice of the final reconstruction (Fig. 6A, B), where two linear densities correspond to the hydrophilic lipid polar heads encompassing the darker hydrophobic core of the plasma membrane. The continuity of the lipid membrane, displaying two clearly defined leaflets demonstrates the efficacy of our STA strategy in sorting out spherules morphological heterogeneity. Our reconstruction exposes a pronounced negative curvature of the PM at the base of the neck, with an average angle of 65 degrees. Additional protein densities are tightly associated with the lipid bilayer at the neck's base, extending towards the cytoplasmic side. This neck complex is composed of three regions: a membrane-bound ring, a barrel-like density composed of three stacked rings present in the cytoplasmic moiety and a central elongated density passing throughout all the rings. The first membrane-bound ring has an outer and inner diameter of 19 nm and 8 nm respectively and displays a tilted "C-like" shaped density

where the opening of the “C” points toward the PM (Fig. 6B). The membrane-bound ring-like density evidenced in our reconstruction perfectly fits with the recently reported atomic structure of the nsP1 dodecameric ring (Fig. 6C-E) (31, 32, 41). The conical shape of the ring exhibiting a larger, flared base is related to the tilted arrangement of nsP1 in the dodecamer. The fact that the dodecameric nature of the nsP1 ring is not apparent in our reconstruction is likely attributable to the lack of particles corresponding to axial or top views of the spherules in our dataset. These top views are consistently associated with spherules positioned atop the cells, where thicker ice leads to a significantly lower signal-to-noise ratio, making it difficult to reliably align particles. It is worth noting that while the PM outer layer has a continuous organization, the inner layer engages in extended contact with nsP1 (Fig.6E). This is in agreement with the role depicted for membrane-binding and oligomerization (MBO) loops 1 and 2, corresponding to nsP1 amino-acids 200-238 and 405-430 respectively in the recombinant nsP1 ring, that forms amphipathic membrane-binding spikes penetrating by about 10 Å into detergent FC12 micelles. This tight interaction is proposed to be reinforced by a triad of palmitoylated cysteines in MBO loop 2 (32). Nevertheless, our observations support additional interactions of nsP1 residues on the outermost domains of the nsP1 ring with PM phospholipids. Going throughout the nsP1 ring, a second central and elongated complex displays two prominent densities, one located on the spherule side and the other more pronounced located in the cytoplasmic part. The stoichiometry of individual compounds involved in this elongated 20 nm density could not be determined from our reconstruction. Finally, surrounding the cytoplasmic part of this central density, the additional barrel-like assembly composed of three stacked rings (~11 nm length / 3.5 nm width) does not show obvious direct interaction with the nsP1 ring or the central elongated complex. This picture identifies CHIKV spherules as composed of two superimposed ring structures, one of which fits with a nsP1 dodecamer, and of central elongated densities. Based on recent biochemical

approaches, the latter may correspond to nsP2 and nsP4 proteins (41) while nsP3 may contribute to the assembly of the cytoplasmic ring-like structure (Fig 6F).

Discussion

In the present study, we investigated the native structural organization of CHIKV ROs in their cellular context using *in situ* cryo-EM approaches. With the aim to decipher the dynamic fate of these compartments, we examined human epithelial cells infected for 17h, a late time point at which multiple infectious cycles have occurred. In this context, we used a fully infectious strain of CHIKV, which required cell fixation with PFA prior to imaging, as it is classically performed with highly infectious viruses (67, 68). This strategy revealed numerous intact cells with unaltered membrane-bound bulb-shaped organelles mainly persisting at the PM at late infection time. This result attests to the poor internalization capacity of these compartments as reported by others (40) and contrasts with the rapid endocytosis, within 3-6h of infection, of PM-derived ROs observed in cells infected with some other Old World alphaviruses including Sindbis virus (SINV) or Semliki Forest virus (SFV). CHIKV ROs were observed at the membrane of the cell body and, contrasting with SINV (57), also on filopodia-like protrusions. In many places, ROs colocalized with budding viral particles and with patches of membrane-anchored densities beneath the plasma membrane attributed to a lattice of CHIKV envelope glycoproteins delivered to the budding sites (69). This colocalization indicates that spherule formation and viral particle budding can happen concomitantly at the same site on virus-induced cell extensions and are therefore not mutually exclusive. Interestingly, looking closer at the organization of spherules, additional densities were often found inserted in ROs delimiting membranes. The use of alphavirus *trans*-replication systems established that SFV spherule biogenesis and growth only require the expression of non-structural proteins and viral RNA synthesis (70). This model was confirmed for CHIKV (71). The occasional presence of envelope glycoproteins at the surface of ROs therefore appears incidental, reflecting the lack of compartmentalization of replication and budding events at a late stage of infection. In the absence of peculiarity regarding their size, morphology, and presence of

compacted RNA in their lumen, ROs with extra densities at their surface are likely functional. While unexpected, recent immunolabelling studies reported the presence of anti-E2 antibody staining at the surface of CHIKV spherules (61). Together with this observation, our results raise the question of the possible functional consequences of such incorporation. Direct cell-to-cell transport of budded particles to uninfected human or mosquito cells by cell extensions involving the E2 envelope glycoprotein was previously reported (72, 73). Hence, the question of an eventual direct way for cell-to-cell transmission of CHIKV genetic material through filopodia is still open.

Surprisingly, CHIKV spherules imaged in the current study, whatever their localization on the PM, are highly heterogeneous in size, with a diameter ranging from 40 to 142 nm (median of 90 nm). A closer analysis of CHIKV ROs size distribution revealed at least three main categories, where ROs displaying diameters of 84-100 nm represented >60% of total events, while compartments with a size of 40-83 nm or 101-152 nm were more rarely detected. Initial observations performed on CHIKV and other model alphaviruses (i.e. SFV and SINV) reported rather homogeneous diameters for ROs ranging from 50 to 70 nm observed at 6-8 hpi (41, 63), a time point corresponding to the completion of a single viral cycle. Using *trans*-replication systems, the size of ROs was correlated with the length of RNA replicated and segregated in these compartments (7, 38) and the ~58 nm spherules formed in SFV-infected cells were proposed to contain a single copy of the viral genome in double-stranded form. Despite having a genome of comparable size, CHIKV replication compartments may behave differently. Indeed, a recent analysis of hamster cells transduced with CHIKV replicons bearing a truncated genome devoid of structural genes revealed ROs size of 50-70 nm (74). Together with the study of Jin et al. (61) reporting spherules up to 132 nm in diameter observed in human cells 10 h after infection, our results reveal the peculiarity of ROs assembled at late stage by a complete infectious CHIKV genome. Considering that the

570 spherule adjusts its size in response to the pressure exerted by the confined nucleic acid, and
571 that we observed a visually similar RNA compaction state regardless of the size of CHIKV
572 ROs, larger spherules may therefore correspond to compartments in which viral RNA
573 continues accumulating. According to this hypothesis, CHIKV spherules may be maintained
574 in an active state at the PM beyond a single RNA replication/transcription cycle. As this
575 assumption relies on a functional state of the CHIKV replication complex, we investigated the
576 structural organization of the spherule neck. Cryo-EM and cryo-ET both revealed a density
577 that separates the RO lumen from the cell cytoplasmic compartment whatever the size of the
578 spherule. Our sub-tomogram averaging approach unveiled that this density corresponds to a
579 membrane-bound ring forming the base of a crown, a structural feature also found for FHV
580 (7, 8) or SARS-CoV-2 (13) replication organelles. The ring fits decently the high resolution
581 nsP1 dodecameric structure obtained by single particle analysis (31, 32) while two other
582 major structural features, namely a cytoplasmic tripartite ring and a central elongated plug
583 density passing through the rings are noticeable. While technical constraints such as sample
584 thickness, spherules heterogeneity and the lack of spherule top views prevented us from
585 achieving a resolution that would allow us to unambiguously assign all visible densities to
586 specific nsPs, our structure exhibits all three characteristic architectural components of the
587 replication complex that have been recently described using recombinant CHIKV nsP1, nsP2
588 and nsP4 encoded by the O'nyong-nyong alphavirus (41) or from cells infected with self-
589 limiting single-cycle CHIKV replicon particles (63). These complexes displayed a
590 proteinaceous ring attributed to nsP1, a central elongated plug density corresponding to the
591 viral polymerase nsP4 facing the RO lumen, the nsP2 helicase-protease facing the cell
592 cytoplasm, and a cytoplasmic barrel-like ring which is proposed to consist of nsP3 and
593 associated cellular factors (41). Our sub-tomogram reconstruction of the RO neck therefore
594 suggests that the crown-like organization of the replication complex persists in ROs

maintained at the PM, arguing for the late functionality of these compartments in viral RNA replication. Determining the RNA species and copy number packaged in the various spherule types remains a crucial but challenging undertaking. Nevertheless, according to the presence of apparently fully mature nsPs at their neck and of the reported regulation of alphavirus replicase activity along nsPs maturation, enlarged ROs are expected to accumulate (+)RNA and more likely sgRNA. In this context, it would also be insightful to explore whether the size of SFV or SINV ROs similarly increases at longer infection times to question potential differences with CHIKV replication mechanisms.

Besides the nsP1 crown gating the entry of the ROs and additional central densities attributed to nsP2 and nsP4, our sub-tomogram average revealed the presence of a crown-like assembly in the cytoplasmic side of spherules. This structure is very similar to the cytoplasmic assembly recently reported by others (41, 63). Nevertheless, the full crown organization of the complex is often difficult to distinguish in individual RO sub-tomograms, with some but not all characteristic structural features visible at once, suggesting some degree of structural dynamics. Hence, the sub-tomogram averaging approach provides a general overview of the late CHIKV replication complex organization that does not however distinguish between all potential functional and structural states of the complex resulting from its dynamical nature.

Strikingly, filamentous densities resembling RNA or ribosome-decorated-like RNA were exclusively observed extruding from ROs exhibiting diameters larger than 90 nm. The presence of decorated RNAs exclusively on ROs larger than 90 nm suggests a late local translating activity. It is worth noting that RNA filamentous densities associated with ROs have been rarely reported by others from CHIKV-infected cells (41, 63) whereas they are clearly visible with Flockhouse nodavirus (FHV) (7). The nature of filaments exported from ROs remains to be investigated (31, 32). Hence, our observation consolidates the proposed idea of sequential models where spherules would first complete (-)RNA synthesis and reach

an optimal size before the replication complex switches its activity to transcription and export of (+) stranded genomic and subgenomic RNAs (40, 56). Of note, when visible, a single filament was observed beneath the spherule, contrasting with the assumed activity of nsP1 dodecamer in the simultaneous capping and export of multiple RNAs.

Surprisingly, the variability of RO diameters at the PM contrasts with their uniform size in CPVs (50-60 nm). This similarity in size to previously reported CHIKV ROs detected at the PM around 6-8 hpi (41, 63) argues for a marginal but temporally regulated internalization mechanism. Internalization and trafficking of alphavirus viral replication complexes are regulated by the phosphatidylinositol-3-kinase (PI3K)-Akt-mammalian target of rapamycin (mTOR) signaling pathway activated by nsP3 (40). However, this activation is inefficient for CHIKV, resulting in the predominant localization of ROs at the cell periphery. The consistent size of internalized ROs implies that internalization likely occurs when spherules reach an optimal size or when nsPs accumulate at a specific concentration in the cytoplasm. Interestingly, the rare CPVs observed in our study localized near cytoplasmic honeycomb assemblies have never been reported so far. These structured arrangements, observed as highly organized globular and tubular structures in thin plastic sections, prompt questions regarding their role in the CHIKV viral cycle. This observation suggests that internalization may not be incidental but rather serve a functional purpose for CHIKV. Therefore, understanding the nature and function of these complexes, absent in non-infected control cells, warrants further investigation.

Altogether, our Cryo-EM and Cryo-ET analyses of CHIKV-infected human cells provides detailed insights into the specifics of CHIKV ROs. These bulb-shaped membranous compartments containing a dynamic fully mature crown-like replication complex at their neck regions are maintained at the PM in a likely functionally active state beyond the theoretical completion of a single RNA replication/transcription cycle. Furthermore, our findings reveal

unexpected characteristics of CHIKV spherules, including size heterogeneity suggestive of continuous nucleic acid accumulation, and the presence of additional membrane-associated densities, possibly indicating the insertion of envelope glycoproteins into the delimiting membrane. We also show that some RNA molecules are released individually from these compartments, attracting protein complexes in the vicinity of the spherules. Interestingly, a marginal subset of spherules with diameters ranging from 50 to 70 nanometers appear to undergo regulated internalization into CPVs, which are often found near honeycomb arrangements, raising questions about the functional significance of CHIKV internalization. These findings provide novel insights into the dynamic behavior and fate of CHIKV ROs in human cells, enhancing our understanding of the Chikungunya viral cycle.

Supplemental material

Girard-etal-Suppl-Fig-1-2.pdf

Acknowledgments

The work was supported by a grant from the French Agence Nationale de la Recherche (ANR-18-CE11-002 to LB and PB). JG has a doctoral fellowship from ANR-18-CE11-002 and *la Fondation pour la Recherche Médicale* (FRM FDT202106013092). CBS is a member of the French Infrastructure for Integrated Structural Biology (FRISBI) supported by Agence Nationale de la Recherche (ANR-10-INBS-05).

Author contributions

P.B. and L.B. designed the study and obtained the funding for the project. J.G., O.LB., J.L-K-H., M.G., E.B., C.C., A.N., A-L. F., L.B., P.B. performed the experiments. J.G., P.B., L.B., J.L-K-H., O.LB., M.C., A-L.F., M.G., X.H. participated to the discussion and interpretation of

the results. X.H., A-L.F., M.G., D.S., O.LB supervised Titan Krios acquisitions. P.B. and L.B. wrote the manuscript helped by the contribution of J.G., O.LB., M.G., A-L.F.

References

1. Grimley PM, Berezesky IK, Friedman RM. 1968. Cytoplasmic structures associated with an arbovirus infection: loci of viral ribonucleic acid synthesis. J Virol 2:1326–1338.
2. Kujala P, Ikäheimonen A, Ehsani N, Vihinen H, Auvinen P, Kääriäinen L. 2001. Biogenesis of the Semliki Forest Virus RNA Replication Complex. J Virol 75:3873–3884.
3. Froshauer S, Kartenbeck J, Helenius A. 1988. Alphavirus RNA replicase is located on the cytoplasmic surface of endosomes and lysosomes. Journal of Cell Biology 107:2075–2086.
4. Paul D. 2013. Architecture and biogenesis of plus-strand RNA virus replication factories. WJV 2:32.
5. Risco C, De Castro IF, Sanz-Sánchez L, Narayan K, Grandinetti G, Subramaniam S. 2014. Three-Dimensional Imaging of Viral Infections. Annu Rev Virol 1:453–473.
6. Kopek BG, Perkins G, Miller DJ, Ellisman MH, Ahlquist P. 2007. Three-Dimensional Analysis of a Viral RNA Replication Complex Reveals a Virus-Induced Mini-Organelle. PLoS Biol 5:e220.
7. Ertel KJ, Benefield D, Castaño-Diez D, Pennington JG, Horswill M, den Boon JA, Otegui MS, Ahlquist P. 2017. Cryo-electron tomography reveals novel features of a viral RNA replication compartment. eLife 6:e25940.
8. Unchwaniwala N, Zhan H, Pennington J, Horswill M, den Boon JA, Ahlquist P. 2020. Subdomain cryo-EM structure of nodaviral replication protein A crown complex provides mechanistic insights into RNA genome replication. Proc Natl Acad Sci USA 117:18680–18691.
9. Welsch S, Miller S, Romero-Brey I, Merz A, Bleck CKE, Walther P, Fuller SD, Antony C, Krijnse-Locker J, Bartenschlager R. 2009. Composition and Three-Dimensional Architecture of the Dengue Virus Replication and Assembly Sites. Cell Host & Microbe 5:365–375.
10. Gillespie LK, Hoenen A, Morgan G, Mackenzie JM. 2010. The Endoplasmic Reticulum Provides the Membrane Platform for Biogenesis of the Flavivirus Replication Complex. J Virol 84:10438–10447.
11. Knoops K, Kikkert M, Worm SHE van den, Zevenhoven-Dobbe JC, van der Meer Y, Koster AJ, Mommaas AM, Snijder EJ. 2008. SARS-Coronavirus Replication Is Supported by a Reticulovesicular Network of Modified Endoplasmic Reticulum. PLoS Biol 6:e226.
12. Klein S, Cortese M, Winter SL, Wachsmuth-Melm M, Neufeldt CJ, Cerikan B, Stanifer ML, Boulant S, Bartenschlager R, Chlanda P. 2020. SARS-CoV-2 structure and replication characterized by in situ cryo-electron tomography. Nat Commun 11:5885.
13. Wolff G, Limpens RWAL, Zevenhoven-Dobbe JC, Laugks U, Zheng S, de Jong AWM, Koning RI, Agard DA, Grünewald K, Koster AJ, Snijder EJ, Bárcena M. 2020. A molecular pore spans the double membrane of the coronavirus replication organelle. Science 369:1395–1398.
14. Burt FJ, Chen W, Miner JJ, Lenschow DJ, Merits A, Schnettler E, Kohl A, Rudd PA, Taylor A, Herrero LJ, Zaid A, Ng LFP, Mahalingam S. 2017. Chikungunya virus: an update on the biology and pathogenesis of this emerging pathogen. The Lancet Infectious Diseases 17:e107–e117.
15. Chevillon C, Briant L, Renaud F, Devaux C. 2008. The Chikungunya threat: an ecological and evolutionary perspective. Trends in Microbiology 16:80–88.
16. Silva LA, Dermody TS. 2017. Chikungunya virus: epidemiology, replication, disease

mechanisms, and prospective intervention strategies. Journal of Clinical Investigation 127:737–749.
17. Wahid B, Ali A, Rafique S, Idrees M. 2017. Global expansion of chikungunya virus: mapping the 64-year history. International Journal of Infectious Diseases 58:69–76.
18. Galán-Huerta KA, Rivas-Estilla AM, Fernández-Salas I, Farfan-Ale JA, Ramos-Jiménez J. 2015. Chikungunya virus: A general overview. Medicina Universitaria 17:175–183.
19. Ahola T, McInerney G, Merits A. 2021. Alphavirus RNA replication in vertebrate cells, p. 111–156. *In* Advances in Virus Research. Elsevier.
20. Kril V, Aïqui-Reboul-Paviet O, Briant L, Amara A. 2021. New Insights into Chikungunya Virus Infection and Pathogenesis. Annu Rev Virol 8:327–347.
21. Holmes AC, Basore K, Fremont DH, Diamond MS. 2020. A molecular understanding of alphavirus entry. PLoS Pathog 16:e1008876.
22. Strauss JH, Strauss EG. 1994. The alphaviruses: gene expression, replication, and evolution. Microbiol Rev 58:491–562.
23. Peränen J, Laakkonen P, Hyvönen M, Kääriäinen L. 1995. The Alphavirus Replicase Protein nsP1 Is Membrane-Associated and Has Affinity to Endocytic Organelles. Virology 208:610–620.
24. Karpe YA, Aher PP, Lole KS. 2011. NTPase and 5′-RNA Triphosphatase Activities of Chikungunya Virus nsP2 Protein. PLoS ONE 6:e22336.
25. Vasiljeva L, Merits A, Auvinen P, Kääriäinen L. 2000. Identification of a Novel Function of the AlphavirusCapping Apparatus. Journal of Biological Chemistry 275:17281–17287.
26. McPherson RL, Abraham R, Sreekumar E, Ong S-E, Cheng S-J, Baxter VK, Kistemaker HAV, Filippov DV, Griffin DE, Leung AKL. 2017. ADP-ribosylhydrolase activity of Chikungunya virus macrodomain is critical for virus replication and virulence. Proc Natl Acad Sci USA 114:1666–1671.
27. Götte B, Liu L, McInerney G. 2018. The Enigmatic Alphavirus Non-Structural Protein 3 (nsP3) Revealing Its Secrets at Last. Viruses 10:105.
28. Hahn YS, Strauss EG, Strauss JH. 1989. Mapping of RNA- temperature-sensitive mutants of Sindbis virus: assignment of complementation groups A, B, and G to nonstructural proteins. J Virol 63:3142–3150.
29. Lemm JA, Bergqvist A, Read CM, Rice CM. 1998. Template-Dependent Initiation of Sindbis Virus RNA Replication In Vitro. J Virol 72:6546–6553.
30. Shirako Y, Strauss JH. 1994. Regulation of Sindbis virus RNA replication: uncleaved P123 and nsP4 function in minus-strand RNA synthesis, whereas cleaved products from P123 are required for efficient plus-strand RNA synthesis. J Virol 68:1874–1885.
31. Zhang K, Law Y-S, Law MCY, Tan YB, Wirawan M, Luo D. 2021. Structural insights into viral RNA capping and plasma membrane targeting by Chikungunya virus nonstructural protein 1. Cell Host & Microbe 29:757-764.e3.
32. Jones R, Bragagnolo G, Arranz R, Reguera J. 2021. Capping pores of alphavirus nsP1 gate membranous viral replication factories. Nature 589:615–619.
33. Ahola T. 1999. Semliki Forest virus mRNA capping enzyme requires association with anionic membrane phospholipids for activity. The EMBO Journal 18:3164–3172.
34. Bakhache W, Neyret A, Bernard E, Merits A, Briant L. 2020. Palmitoylated Cysteines in Chikungunya Virus nsP1 Are Critical for Targeting to Cholesterol-Rich Plasma Membrane Microdomains with Functional Consequences for Viral Genome Replication. J Virol 94:e02183-19.
35. Laakkonen P, Ahola T, Kääriäinen L. 1996. The Effects of Palmitoylation on Membrane Association of Semliki Forest Virus RNA Capping Enzyme. Journal of

Biological Chemistry 271:28567–28571.
36. Spuul P, Salonen A, Merits A, Jokitalo E, Kääriäinen L, Ahola T. 2007. Role of the Amphipathic Peptide of Semliki Forest Virus Replicase Protein nsP1 in Membrane Association and Virus Replication. J Virol 81:872–883.
37. Frolova EI, Gorchakov R, Pereboeva L, Atasheva S, Frolov I. 2010. Functional Sindbis Virus Replicative Complexes Are Formed at the Plasma Membrane. J Virol 84:11679–11695.
38. Kallio K, Hellström K, Balistreri G, Spuul P, Jokitalo E, Ahola T. 2013. Template RNA Length Determines the Size of Replication Complex Spherules for Semliki Forest Virus. J Virol 87:9125–9134.
39. Spuul P, Balistreri G, Hellström K, Golubtsov AV, Jokitalo E, Ahola T. 2011. Assembly of Alphavirus Replication Complexes from RNA and Protein Components in a Novel *trans* -Replication System in Mammalian Cells. J Virol 85:4739–4751.
40. Thaa B, Biasiotto R, Eng K, Neuvonen M, Götte B, Rheinemann L, Mutso M, Utt A, Varghese F, Balistreri G, Merits A, Ahola T, McInerney GM. 2015. Differential Phosphatidylinositol-3-Kinase-Akt-mTOR Activation by Semliki Forest and Chikungunya Viruses Is Dependent on nsP3 and Connected to Replication Complex Internalization. J Virol 89:11420–11437.
41. Tan YB, Chmielewski D, Law MCY, Zhang K, He Y, Chen M, Jin J, Luo D. 2022. Molecular architecture of the Chikungunya virus replication complex. Sci Adv 8:eadd2536.
42. Kümmerer BM, Grywna K, Gläsker S, Wieseler J, Drosten C. 2012. Construction of an infectious Chikungunya virus cDNA clone and stable insertion of mCherry reporter genes at two different sites. Journal of General Virology 93:1991–1995.
43. Vanlandingham DL, Tsetsarkin K, Hong C, Klingler K, McElroy KL, Lehane MJ, Higgs S. 2005. Development and characterization of a double subgenomic chikungunya virus infectious clone to express heterologous genes in Aedes aegypti mosqutioes. Insect Biochemistry and Molecular Biology 35:1162–1170.
44. Bernard E, Solignat M, Gay B, Chazal N, Higgs S, Devaux C, Briant L. 2010. Endocytosis of Chikungunya Virus into Mammalian Cells: Role of Clathrin and Early Endosomal Compartments. PLoS ONE 5:e11479.
45. Schneider CA, Rasband WS, Eliceiri KW. 2012. NIH Image to ImageJ: 25 years of image analysis. Nat Methods 9:671–675.
46. Hagen WJH, Wan W, Briggs JAG. 2017. Implementation of a cryo-electron tomography tilt-scheme optimized for high resolution subtomogram averaging. Journal of Structural Biology 197:191–198.
47. Nicastro D. 2009. Cryo-Electron Microscope Tomography to Study Axonemal Organization, p. 1–39. *In* Methods in Cell Biology. Elsevier.
48. Zheng SQ, Palovcak E, Armache J-P, Verba KA, Cheng Y, Agard DA. 2017. MotionCor2: anisotropic correction of beam-induced motion for improved cryo-electron microscopy. Nat Methods 14:331–332.
49. Kremer JR, Mastronarde DN, McIntosh JR. 1996. Computer visualization of three-dimensional image data using IMOD. J Struct Biol 116:71–76.
50. Hoenger A. 2014. High-resolution cryo-electron microscopy on macromolecular complexes and cell organelles. Protoplasma 251:417–427.
51. Xiong Q, Morphew MK, Schwartz CL, Hoenger AH, Mastronarde DN. 2009. CTF determination and correction for low dose tomographic tilt series. Journal of Structural Biology 168:378–387.
52. Grant T, Grigorieff N. 2015. Measuring the optimal exposure for single particle cryo-EM using a 2.6 Å reconstruction of rotavirus VP6. eLife 4:e06980.

53. Tang G, Peng L, Baldwin PR, Mann DS, Jiang W, Rees I, Ludtke SJ. 2007. EMAN2: An extensible image processing suite for electron microscopy. Journal of Structural Biology 157:38–46.
54. Chen M, Bell JM, Shi X, Sun SY, Wang Z, Ludtke SJ. 2019. A complete data processing workflow for cryo-ET and subtomogram averaging. Nat Methods 16:1161–1168.
55. Goddard TD, Huang CC, Ferrin TE. 2007. Visualizing density maps with UCSF Chimera. Journal of Structural Biology 157:281–287.
56. Spuul P, Balistreri G, Kääriäinen L, Ahola T. 2010. Phosphatidylinositol 3-Kinase-, Actin-, and Microtubule-Dependent Transport of Semliki Forest Virus Replication Complexes from the Plasma Membrane to Modified Lysosomes. J Virol 84:7543–7557.
57. Jose J, Taylor AB, Kuhn RJ. 2017. Spatial and Temporal Analysis of Alphavirus Replication and Assembly in Mammalian and Mosquito Cells. mBio 8:e02294-16.
58. Gorchakov R, Garmashova N, Frolova E, Frolov I. 2008. Different Types of nsP3-Containing Protein Complexes in Sindbis Virus-Infected Cells. J Virol 82:10088–10101.
59. Laakkonen P, Auvinen P, Kujala P, Kääriäinen L. 1998. Alphavirus Replicase Protein NSP1 Induces Filopodia and Rearrangement of Actin Filaments. J Virol 72:10265–10269.
60. Chmielewski D, Schmid MF, Simmons G, Jin J, Chiu W. 2022. Chikungunya virus assembly and budding visualized in situ using cryogenic electron tomography. Nat Microbiol 7:1270–1279.
61. Jin J, Galaz-Montoya JG, Sherman MB, Sun SY, Goldsmith CS, O'Toole ET, Ackerman L, Carlson L-A, Weaver SC, Chiu W, Simmons G. 2018. Neutralizing Antibodies Inhibit Chikungunya Virus Budding at the Plasma Membrane. Cell Host & Microbe 24:417-428.e5.
62. Pietilä MK, van Hemert MJ, Ahola T. 2018. Purification of Highly Active Alphavirus Replication Complexes Demonstrates Altered Fractionation of Multiple Cellular Membranes. J Virol 92:e01852-17.
63. Laurent T, Kumar P, Liese S, Zare F, Jonasson M, Carlson A, Carlson L-A. 2022. Architecture of the chikungunya virus replication organelle. eLife 11:e83042.
64. Al-Amoudi A, Chang J-J, Leforestier A, McDowall A, Salamin LM, Norlén LPO, Richter K, Blanc NS, Studer D, Dubochet J. 2004. Cryo-electron microscopy of vitreous sections. EMBO J 23:3583–3588.
65. Mahamid J, Pfeffer S, Schaffer M, Villa E, Danev R, Kuhn Cuellar L, Förster F, Hyman AA, Plitzko JM, Baumeister W. 2016. Visualizing the molecular sociology at the HeLa cell nuclear periphery. Science 351:969–972.
66. Nishikiori M, Den Boon JA, Unchwaniwala N, Ahlquist P. 2022. Crowning Touches in Positive-Strand RNA Virus Genome Replication Complex Structure and Function. Annu Rev Virol 9:193–212.
67. Mattei S, Glass B, Hagen WJH, Kräusslich H-G, Briggs JAG. 2016. The structure and flexibility of conical HIV-1 capsids determined within intact virions. Science 354:1434–1437.
68. Ke Z, Oton J, Qu K, Cortese M, Zila V, McKeane L, Nakane T, Zivanov J, Neufeldt CJ, Cerikan B, Lu JM, Peukes J, Xiong X, Kräusslich H-G, Scheres SHW, Bartenschlager R, Briggs JAG. 2020. Structures and distributions of SARS-CoV-2 spike proteins on intact virions. Nature 588:498–502.
69. Soonsawad P, Xing L, Milla E, Espinoza JM, Kawano M, Marko M, Hsieh C, Furukawa H, Kawasaki M, Weerachatyanukul W, Srivastava R, Barnett SW, Srivastava IK, Cheng RH. 2010. Structural Evidence of Glycoprotein Assembly in Cellular

Membrane Compartments prior to Alphavirus Budding. J Virol 84:11145–11151.
70. Hellström K, Kallio K, Utt A, Quirin T, Jokitalo E, Merits A, Ahola T. 2017. Partially Uncleaved Alphavirus Replicase Forms Spherule Structures in the Presence and Absence of RNA Template. J Virol 91:e00787-17.
71. Utt A, Quirin T, Saul S, Hellström K, Ahola T, Merits A. 2016. Versatile Trans-Replication Systems for Chikungunya Virus Allow Functional Analysis and Tagging of Every Replicase Protein. PLoS ONE 11:e0151616.
72. Lee CY, Kam Y-W, Fric J, Malleret B, Koh EGL, Prakash C, Huang W, Lee WWL, Lin C, Lin RTP, Renia L, Wang C-I, Ng LFP, Warter L. 2011. Chikungunya Virus Neutralization Antigens and Direct Cell-to-Cell Transmission Are Revealed by Human Antibody-Escape Mutants. PLoS Pathog 7:e1002390.
73. Yin P, Davenport BJ, Wan JJ, Kim AS, Diamond MS, Ware BC, Tong K, Couderc T, Lecuit M, Lai JR, Morrison TE, Kielian M. 2023. Chikungunya virus cell-to-cell transmission is mediated by intercellular extensions in vitro and in vivo. Nat Microbiol 8:1653–1667.
74. Laurent T, Carlson L-A. 2023. The organization of double-stranded RNA in the chikungunya virus replication organelle. PLoS Negl Trop Dis 17:e0011404.

Figure legends

Fig 1. Characterization of CHIKV replication organelles sites

A. Immunofluorescence assays of HEK293T-CHIKV infected cells for 17h at MOI 50. Immunolabeling was performed using mouse monoclonal antibodies against nsP1 (anti-Alexa-488 nsp1 antibody, green channel) and dsRNA (anti Alexa-647-dsRNA antibody, deep red channel represented in grey). nsP3 is detected through the fluorescence of the fused *mCherry* protein (nsP3-mCherry, red channel). Nuclei were stained with DAPI (blue). The colocalization of nsP1, nsP3 and dsRNA reveals the presence of CHIKV replication organelles that are clearly present on the cell membrane of the infected cells (white arrows) and also onto cell filopodia caused by CHIKV infection (yellow arrows). Scale bar, 2.5 µm.

B, C, D and E. Thin sections of HEK293T-CHIKV infected cells for 17h at MOI 50 observed by transmission electron microscopy. CHIKV replication organelles appear as vesicles with diameters ranging from 50 to 100 nm, displaying condensed genetic material within its center (dark arrows) while CHIKV particles appear as smaller electron-dense dark spots (white arrows). Cytopathic vacuoles may occasionally be observed (red square and D) in which CHIKV ROs line the inner surface. A regular array is observed in the vicinity, featuring both particle-shaped structures (red arrows) and tubular structures (blue arrows).

Fig 2. CHIKV replication organelles are observed at the plasma membrane delimiting the cell body and filopodia-like extensions of infected cells.

A, C and E show sections in electron tomogram of HEK293T cell infected for 17h at MOI 50 while **B, D and F** display their corresponding segmentations. Scale bar, 50 nm. Plasma membrane (PM), indicated by brown arrows, delimits the cell membrane (A) and filopodia extensions (C and E) of infected cells. CHIKV replication organelles (light brown arrows) appear as spherules of variable diameter delineated by the PM and connected to the cell by a narrow neck (white arrows). It is sometimes possible to see additional densities on their surface (yellow arrows in E and F). The interior of spherules contains densely packed dsRNA (light blue arrows in E and F). Cytoskeleton filaments present beneath the PM are indicated by purple arrows. The repetitive nature of actin filaments, present as a dense network of filament in filopodia extensions, are clearly visible (low-pass filtered inset in C). Small

isolated densities corresponding to cellular components are also present beneath the PM and indicated by green arrows. CHIKV particles appear as smaller electron-dense particles (red arrows) of about 50-70 nm in diameter. In the vicinity of the viral particles, local thickening of the PM can sometimes be observed (dark blue arrows in E and F).

Fig 3. CHIKV replication organelles diameter distribution.

A. Histogram distribution of ROs diameters computed from spherules located on cell bodies (red; 2,083 measurements) and filopodia-like extensions (green; 950 measurements). The insert shows how the diameter has been determined. Both populations fit with a Gaussian distribution with a mean diameter of 84.2 and 90 nm for cell body and filopodia-like extension ROs respectively. **B.** Histogram distribution of ROs diameters considering all ROs, corresponding to 3033 measurements. Curve-fitting deconvolution unveils eight Gaussian sub-populations whose mean diameters are indicated.

Fig 4. Cryo-EM vitreous sections of CHIKV-infected cells reveal the presence of cytopathic vacuoles.

A and B. Some RO-filled cytopathic vacuoles (CPV) (black arrows), 200 to 500 nm in diameter are observed in vitreous sections. They are delineated by a lipid bilayer and often found in the vicinity of mitochondria (M). Scale bar, 50 nm.

Fig 5. CHIKV ROs display numerous patterns.

Cryo-EM sections of ROs showing the base of spherules and their corresponding segmentations. ROs are displayed according to the diameter of spherules, ranging from 40 to 140 nm (from left to right) and absence (A) or presence (B) of clear associated density patterns, just beneath the PM. The PM is drawn in brown, the spherule membrane in light brown, the additional densities at the surface of some ROs membrane are in yellow, the base of ROs neck in pink, the viral RNA in blue, ribosomes in green, and intracellular filaments in purple. Viral or cell host partners present just beneath the RO neck are in deep blue.

Fig 6. Structural organization of CHIKV RO connection to the plasma membrane revealed by sub-tomogram averaging

A. Surface representation of the 3D reconstruction of the neck of CHIKV ROs (EMDB:EMD-50321). **B.** Central section of the 3D reconstruction. As a visual aid, the location of the spherule membrane is drawn as a white dotted line. The PM appears as two parallel white linear densities encompassing a dark region. Several densities highlighted by the white and black arrows are resolved at the level of the RO neck, as well as a C-shaped density (star) corresponding to the nsP1 ring snuggly interacting with the PM at the base of the neck. **C.** Central section of the surface representation of the RO connection to the PM. The dodecameric nsP1 ring atomic model (PDB: 6Z0V) fits the C-shaped ring density. The central channel is plugged by an elongated central density protruding toward the cell cytoplasm (white arrow) while a second tall barrel-like density composed of three stacked rings (black arrows) shows no apparent connection with other densities. **D.** Surface representation of the map viewed from the interior of the spherule. A ring is present at the base of the spherule in which the dodecameric nsP1 atomic model fits perfectly. **E.** Model of nsP1 ring insertion in the PM internal layer that supports a tight interaction of nsP1 MBO loops with the PM. The insertion of the palmitoyl moieties into the PM is indicated in red. **F.** The structure of the complex composed of nsP1, 2 and 4 (PDB: 7Y38) obtained by Tan et al. by single particle analysis (41) fits well into the 3D map, revealing additional densities forming a barrel around a central density formed in part by nsP2 that could correspond to the contribution of nsP3.

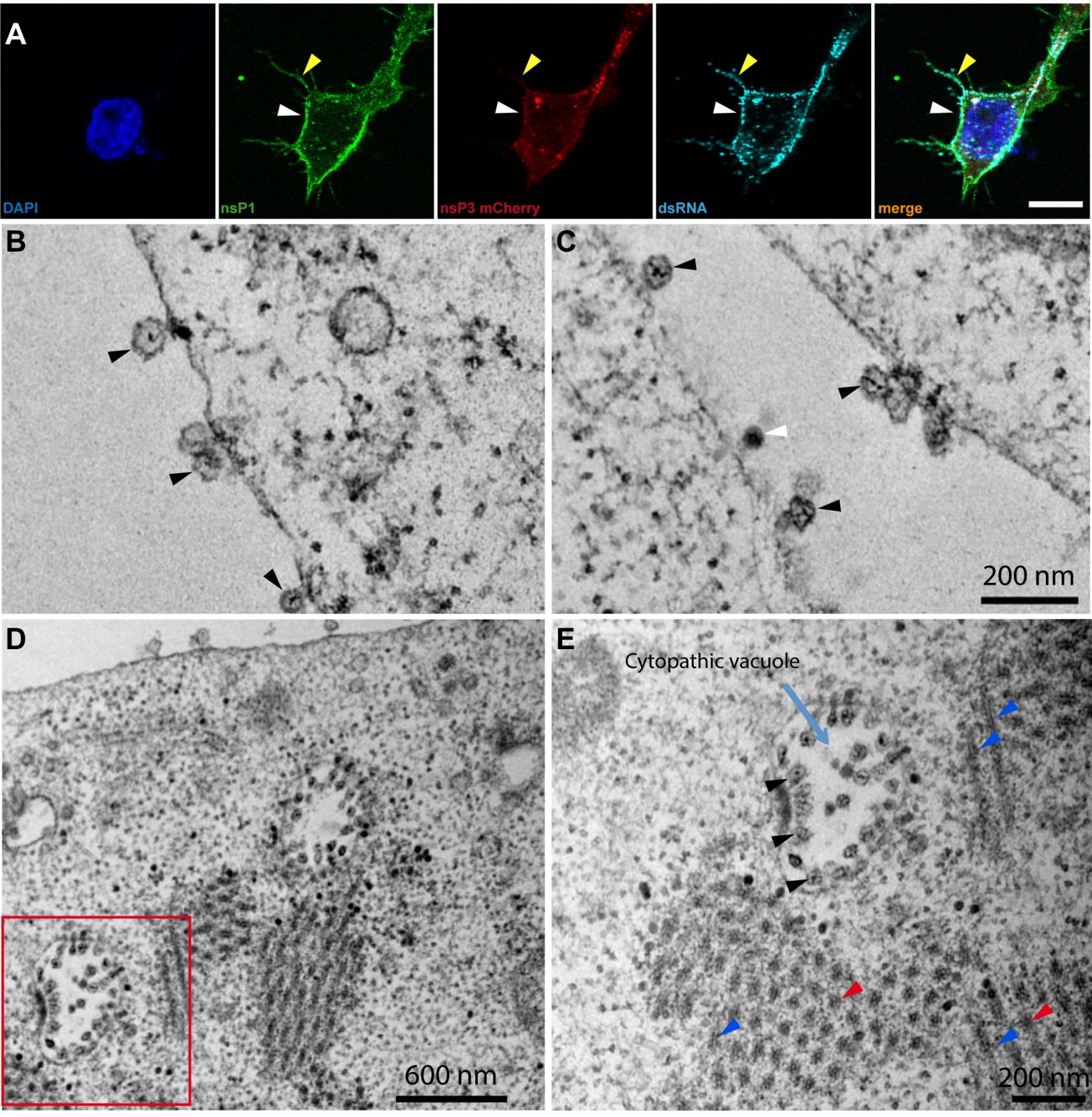
A
DAPI
nsP1
nsP3 mCherry
dsRNA
merge
B
C
200 nm
D
600 nm
E
Cytopathic vacuole
200 nm

Fig. 1

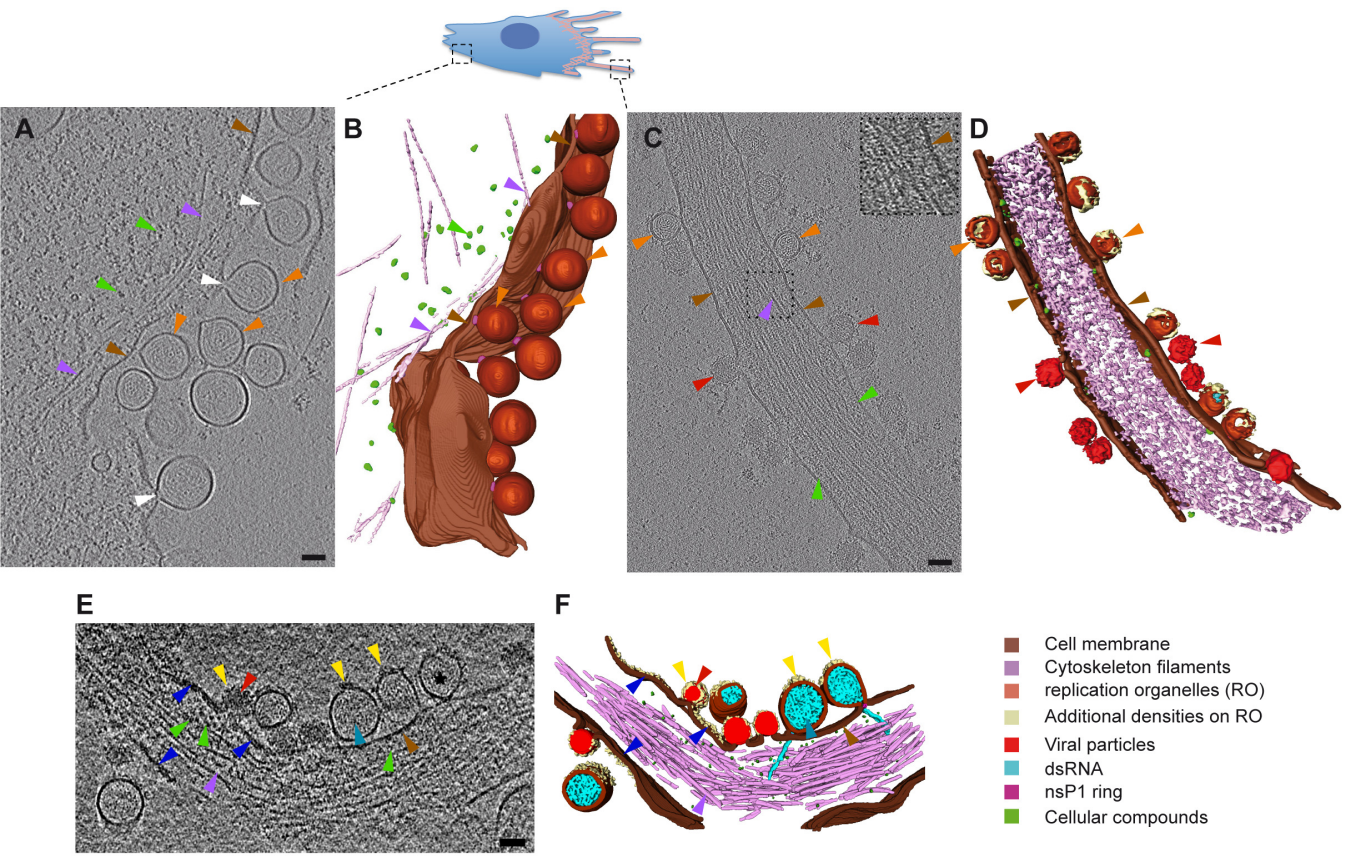
A
B
C
D
E
F
Cell membrane
Cytoskeleton filaments
replication organelles (RO)
Additional densities on RO
Viral particles
dsRNA
nsP1 ring
Cellular compounds

Fig. 2

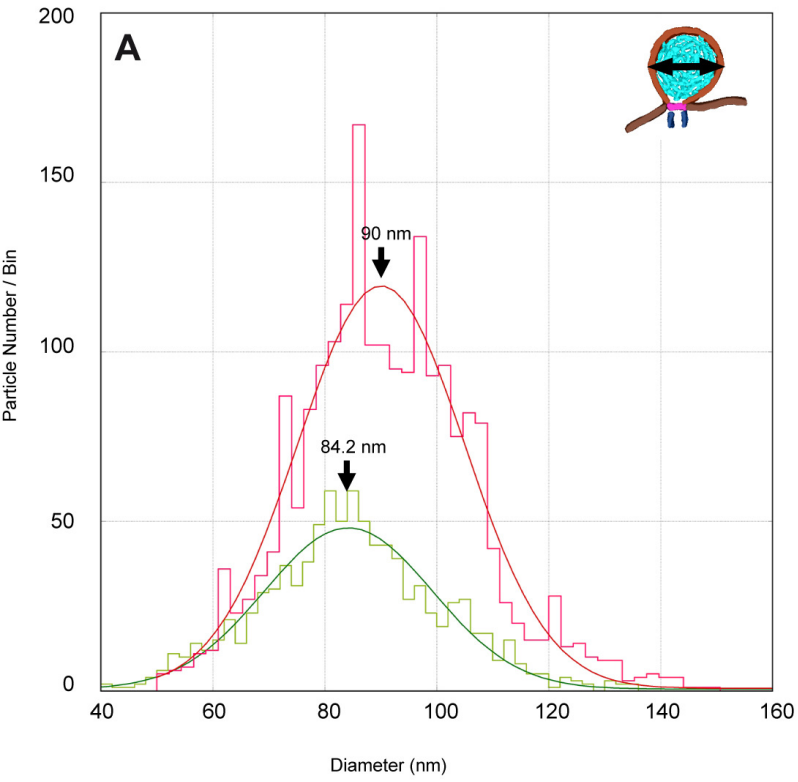
A
90 nm
84.2 nm
Particle Number / Bin
Diameter (nm)
0
50
100
150
200
40
60
80
100
120
140
160

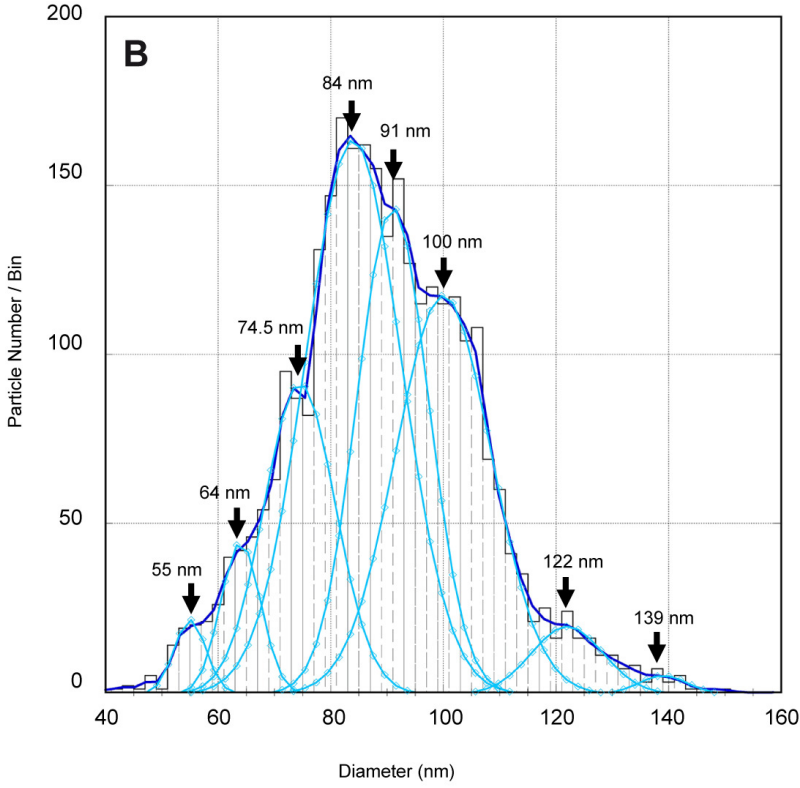
B
84 nm
91 nm
100 nm
74.5 nm
64 nm
55 nm
122 nm
139 nm
Particle Number / Bin
Diameter (nm)
0
50
100
150
200
40
60
80
100
120
140
160

Fig. 3

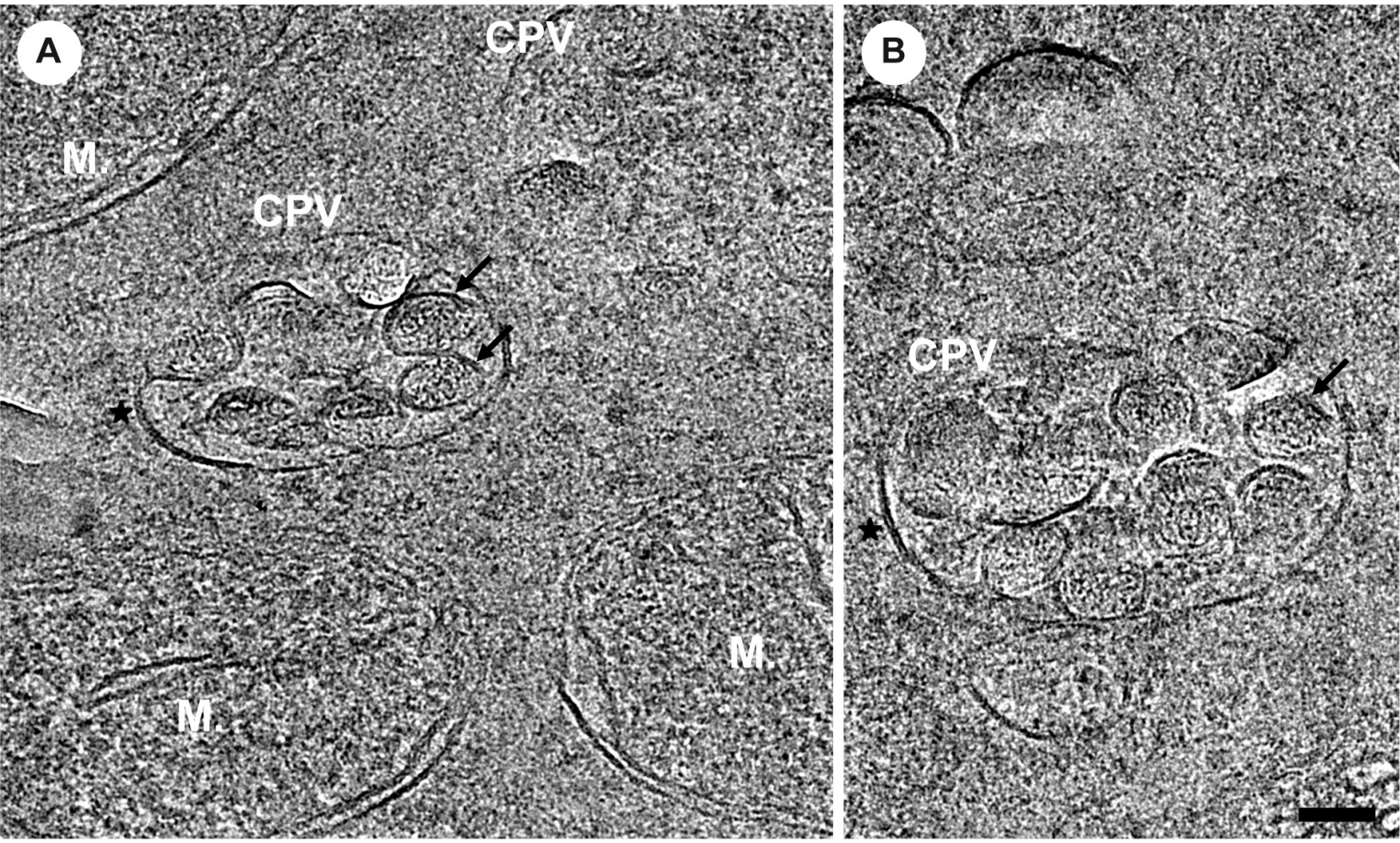

Fig. 4

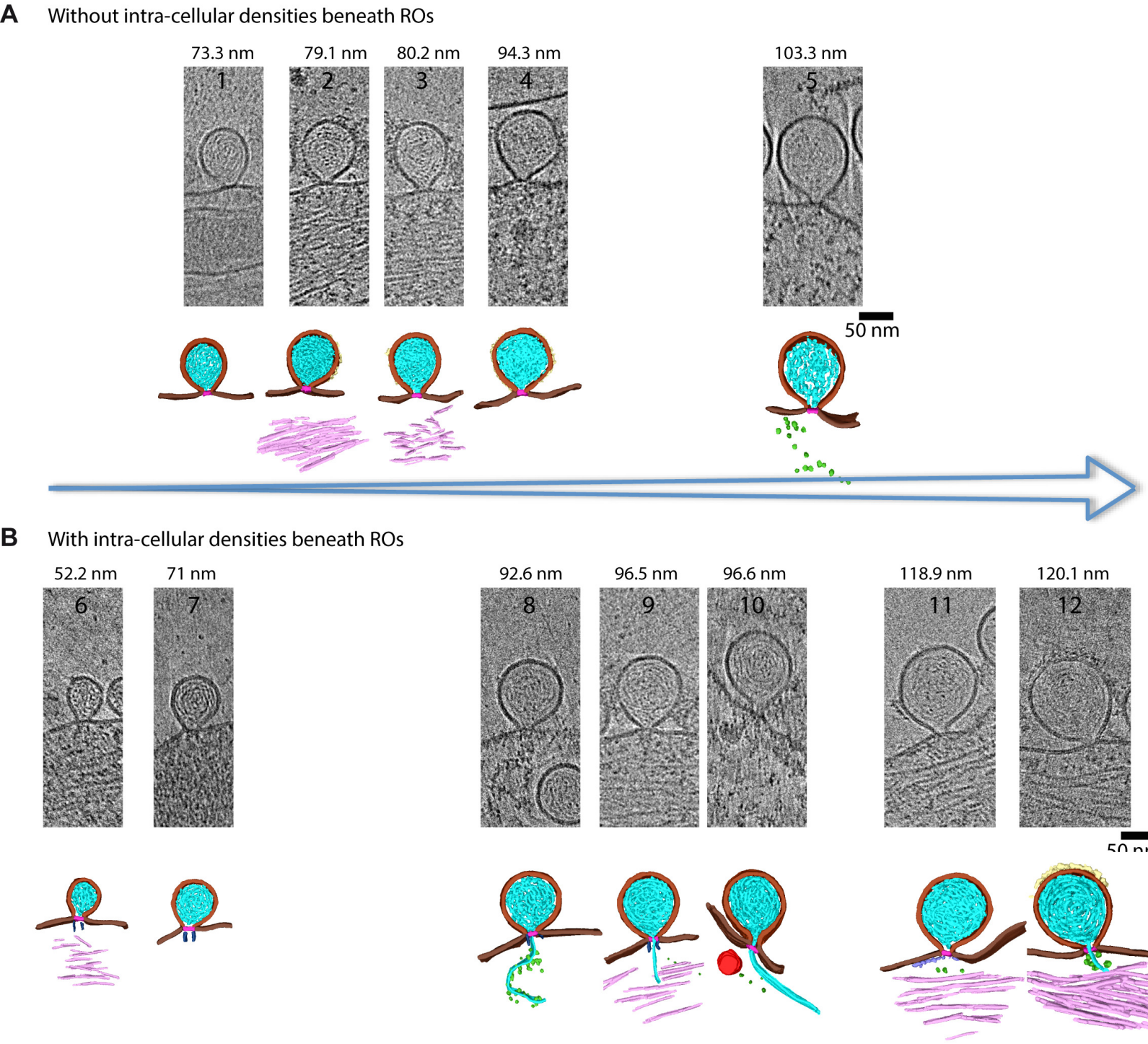
A
Without intra-cellular densities beneath ROs
73.3 nm
79.1 nm
80.2 nm
94.3 nm
103.3 nm
1
2
3
4
5
50 nm
B
With intra-cellular densities beneath ROs
52.2 nm
71 nm
92.6 nm
96.5 nm
96.6 nm
118.9 nm
120.1 nm
6
7
8
9
10
11
12

Fig. 5

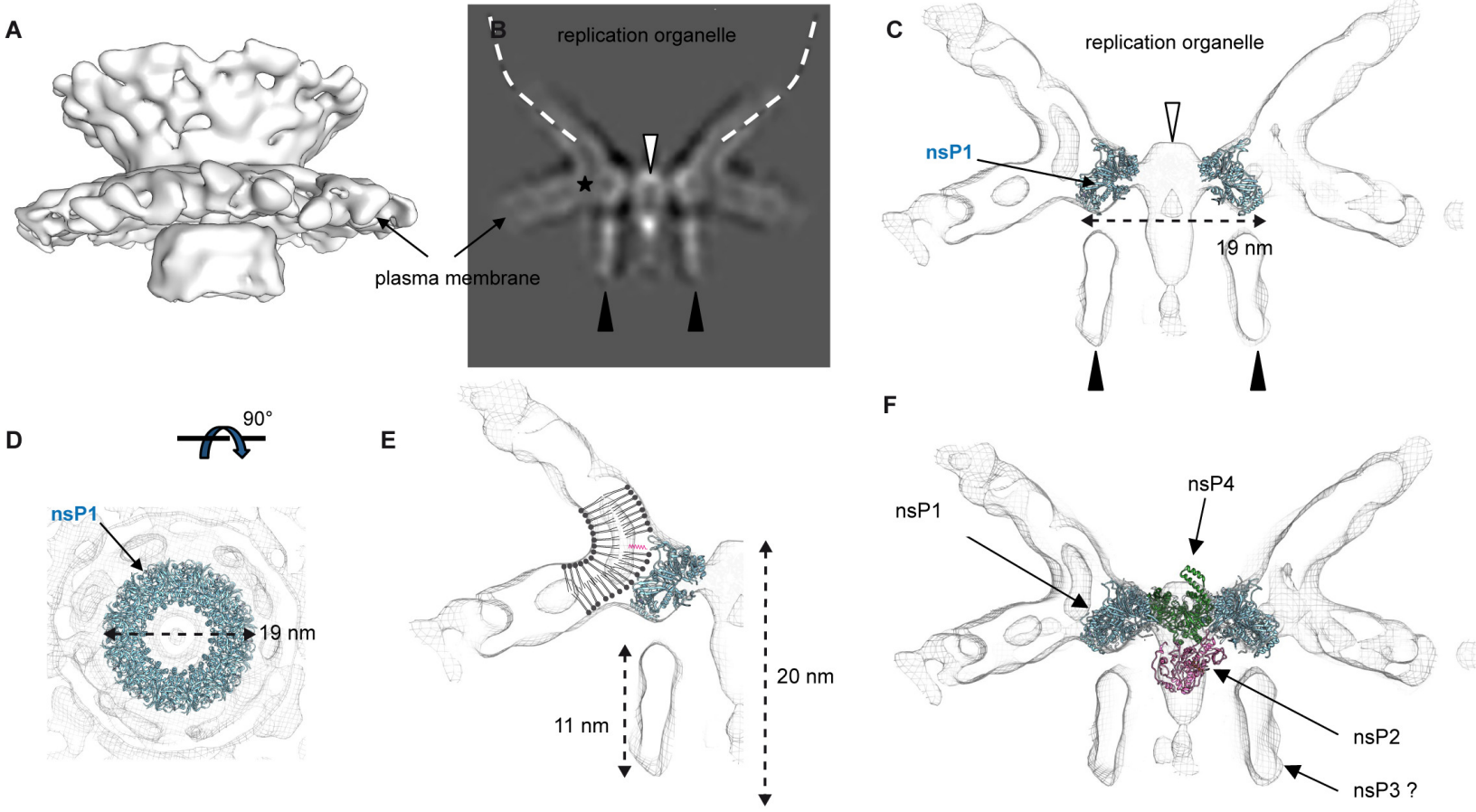
A
B
replication organelle
plasma membrane
C
replication organelle
nsP1
19 nm
D
90°
nsP1
19 nm
E
20 nm
11 nm
F
nsP1
nsP4
nsP2
nsP3 ?

Fig. 6